Electronic Supplementary Information

Tuneable Fluidics within Graphene Nanogaps for Water Purification and Energy Storage

Zheng Bo,[*a] *Yilei Tian,*[a] *Zhao Jun Han,*[b] *Shenghao Wu,*[a] *Shuo Zhang,*[a] *Jianhua Yan,*[a] *Kefa Cen*[a] *and Kostya (Ken) Ostrikov*[c,b,a]

[a]State Key Laboratory of Clean Energy Utilization, College of Energy Engineering, Zhejiang University, Hangzhou, Zhejiang 310027, China

[b]Joint CSIRO-QUT Sustainable Processes and Devices Laboratory, P. O. Box 218, Lindfield, NSW 2070, Australia

[c]School of Chemistry, Physics and Mechanical Engineering, Queensland University of Technology, Brisbane, Queensland 4000, Australia

*) Corresponding author: bozh@zju.edu.cn

Contents

S1. Distinctive features of the proposed approach.

Table S1. Our approach *versus* existing state-of-the-art.

Items	State-of-the-art	Current work
Texture construction	Multi-step process	Single-step process
	Wet-chemistry	Dry-plasma and contaminant free
Texture adjustment	Macro- or micro-scale	Sub-micrometer scale
	Reactive chemistry	Liquid immersion and evaporation
Wettability	Specific type	Adjustable in a wide range
Performance	Specific type	Tunable
Stability	Major changes (315%) of contact angle with ageing [a)]	Stable (~5% change) of contact angle over 90 days

a) Data from literature and re-confirmed in this work (see Sec. S6)

S2. SEM image of Sub-μGWs/O at low-magnification.

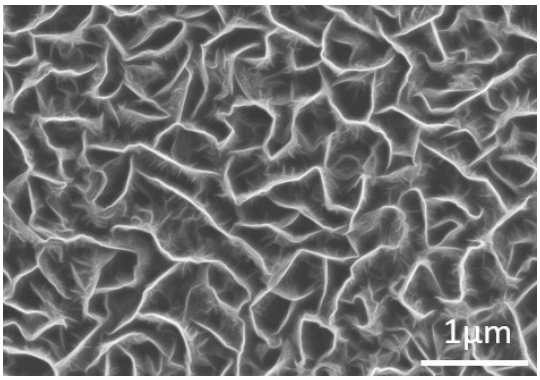

Fig. S1 SEM image of Sub-μGWs/O at low magnification.

S3. TEM and HR-TEM images of Sub-µGWs

To identify the graphene structure of Sub-µGWs, TEM and HRTEM were conducted. The TEM micrograph exhibits graphene's transparent thin nanosheets with wrinkled structure. The interlayer spacing was measured to be approximately 0.35 nm according to the HRTEM examination.

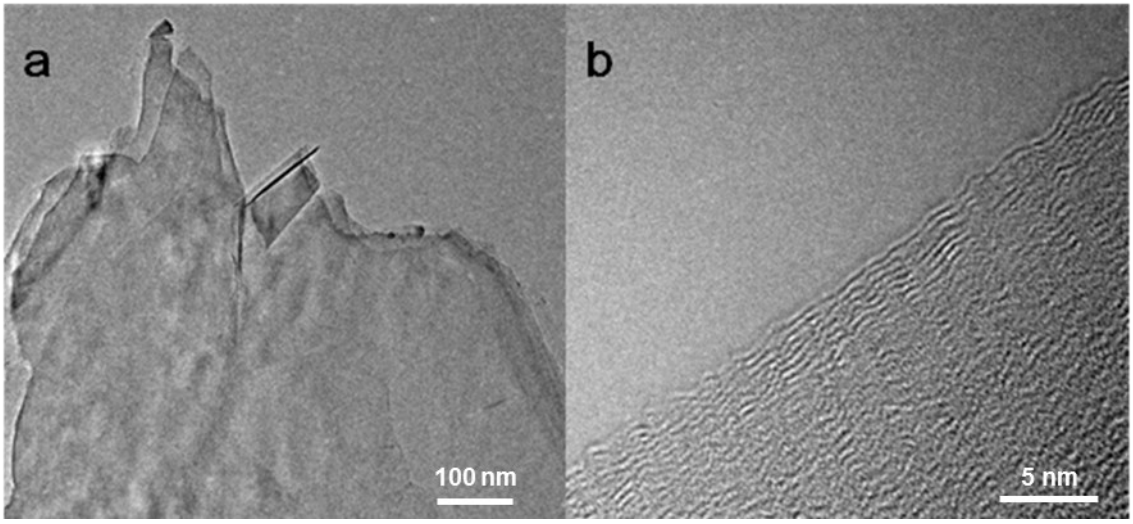

Fig. S2 (a) TEM and (b) HRTEM images of Sub-µGWs.

S4. Variable liquid media.

Ethanol and toluene with different surface tensions (21.97 and 27.93 mN/m, respectively) were used as the alternative liquid media. The produced samples were labeled as Sub-μGWs/E and Sub-μGWs/T, respectively. Fig. S3 shows the representative SEM images and optical microscopy images of the apparent contact angles of Sub-μGWs/E and Sub-μGWs/T. With repeated experiments to minimize statistical errors, the contact angles of Sub-μGWs/E and Sub-μGWs/T were measured as 18.7±2.0° and 92.5±2.9°, respectively.

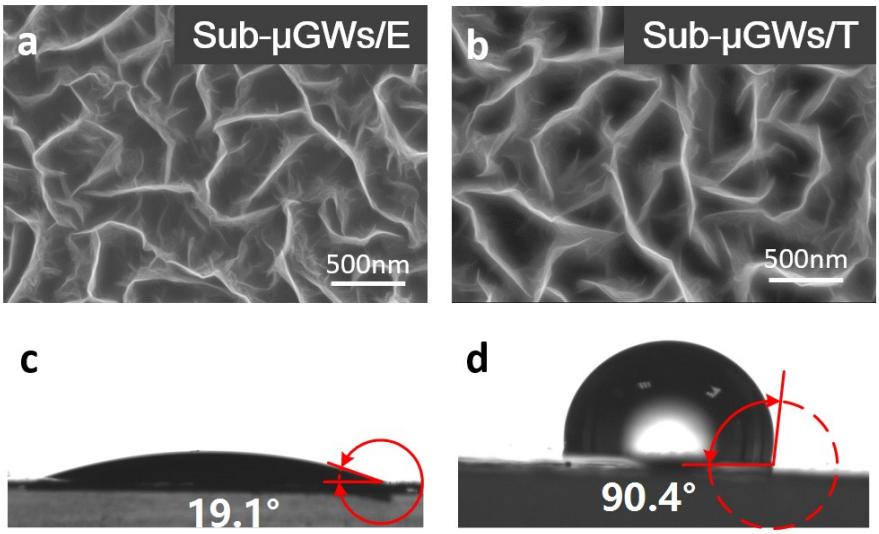

Fig. S3 SEM images of (a) Sub-μGWs/E and (b) Sub-μGWs/T. Optical microscopy images of the apparent contact angles of (c) Sub-μGWs/E and (d) Sub-μGWs/T.

S5. Surface energy calculation.

Calculation of surface energy is based on the Owens-Wendt surface energy theory, which was proposed by Owens[SR1] who extended the Fowkes concept[SR2]. The surface energies of Sub-μGWs/O, Sub-μGWs/A and Sub-μGWs/W were calculated as:

$$\gamma_l(\cos\theta+1)/2 = (\gamma_l^d)^{1/2}\left(\gamma_s^d\right)^{1/2} + \left(\gamma_l^p\right)^{1/2}\left(\gamma_s^p\right)^{1/2} \quad \text{(S1)}$$

$$\gamma_s = \gamma_s^d + \gamma_s^p \quad \text{(S2)}$$

where γ_s is the surface energy, and γ_l^d, γ_l^p, γ_s^d, and γ_s^p are the liquid dispersion component, liquid polar component, solid dispersive component, and solid polar component, respectively. The dispersion and the polar components of the surface free energy of water are 21.8 and 51.0 mJ/m^2, respectively, and those of glycerol are 37.0 and 26.4 mJ/m^2, respectively[SR3]. The water contact angels of Sub-μGWs/O, Sub-μGWs/A and Sub-μGWs/W were presented in the maintext. As shown in Fig. S3, the glycerol contact angles of Sub-μGWs/O, Sub-μGWs/A and Sub-μGWs/W were measured as 8.8°, 51.1° and 103.8°, respectively. The surface energy values of Sub-μGWs/O, Sub-μGWs/A and Sub-μGWs/W were computed as 73.5, 62.4, and 8.9 mJ/m^2, respectively.

Fig. S4 Images of glycerol droplets on the surfaces of (a) Sub-μGWs/O, (b) Sub-μGWs/A and (c) Sub-μGWs/W.

S6. Dynamic droplet impact experiments.

In addition to the static contact angle measurements, dynamic droplet impact experiments were also conducted. Fig. S5a and b show the successive snapshots of the droplet impacting the Sub-μGWs/O and Sub-μGWs/W surfaces, respectively. As for Sub-μGWs/W, the droplet deformed strongly and then a secondary droplet was jetted at its top. This indicates that the hydrophobic Sub-μGWs/W surface allowed the droplet to store its kinetic energy through surface deformation[SR4]. Within the impact, only a small part of energy was consumed by viscous dissipation of the droplet on the hydrophobic Sub-μGWs/W surface, leading to the formation of a secondary droplet detaching from the liquid, *i.e.*, the so-called partial rebound scenario[SR4, 5]. In contrast, due to the superhydrophilic surface of Sub-μGWs/O, the droplet stayed on the surface without the jetting of a secondary droplet, indicating relatively high dissipation of viscous energy during the droplet deformation. Such observations further corroborate the achieved effective tailoring of the surface wetting property.

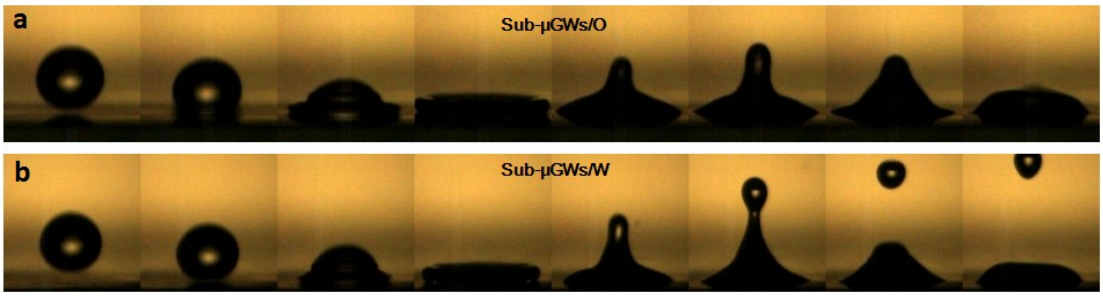

Fig. S5 Successive snapshots of a water droplet hitting the (a) Sub-μGWs/O and (b) Sub-μGWs/W surfaces.

S7. Oxygen plasma treatment.

Sub-μGWs without nanoflaps produced by a conventional RF plasma reactor are hydrophobic with a contact angle of 129.8°, as shown in Fig. S6a. A commercial plasma reactor (Plasmalab System100, Oxford Instruments, UK), as shown in Fig. S6b, was used for the oxygen plasma treatment of Sub-μGWs. Pure oxygen was used and the plasma power was set as 100 W. Oxygen plasma treatment was first conducted at atmospheric pressure for 10 s. Results show that the hydrophobic nature of Sub-μGWs did not change obviously with an apparent contact angle of 123.7°, as shown in Fig. S6c. We further conducted oxygen plasma treatment at relatively lower pressure, i.e., 20 mTorr. As shown in Fig. S6d, the contact angle changed to 8.7° after 10 s. However, such an effect of turning wettability is temporary. The contact angle increased to 12.4° after 3 h, and the ageing effects were getting more obvious with time. After 24 h, the contact angle increased to 27.4°.

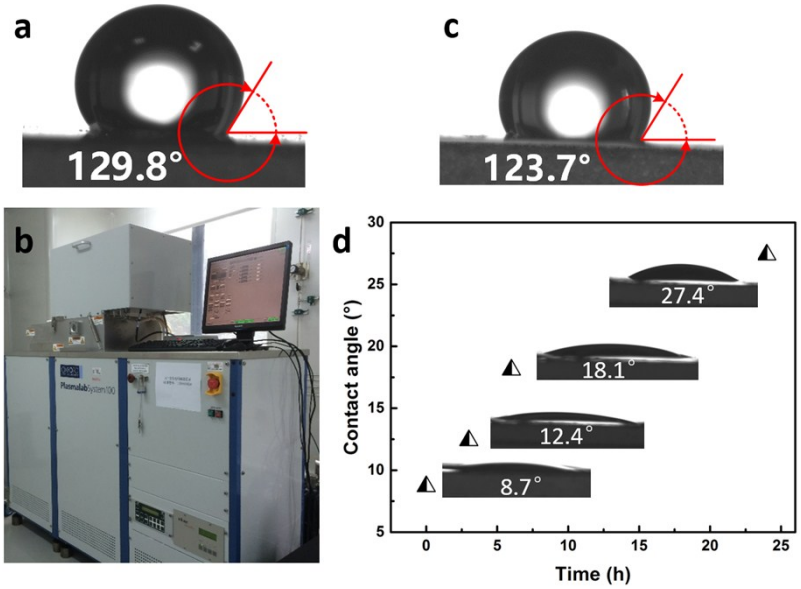

Fig. S6 Optical microscopy images of the apparent contact angles of Sub-μGWs without nano-flaps produced by a conventional RF plasma reactor (a) before and (c) after atmospheric-pressure oxygen plasma treatment. (b) Oxygen plasma reactor. (d) Ageing effect

of low-pressure oxygen plasma treatment. Contact angle changes approx. 315% within 24 hours due to the ageing effect.

S8. X-ray photoelectron spectroscopy (XPS) measurements

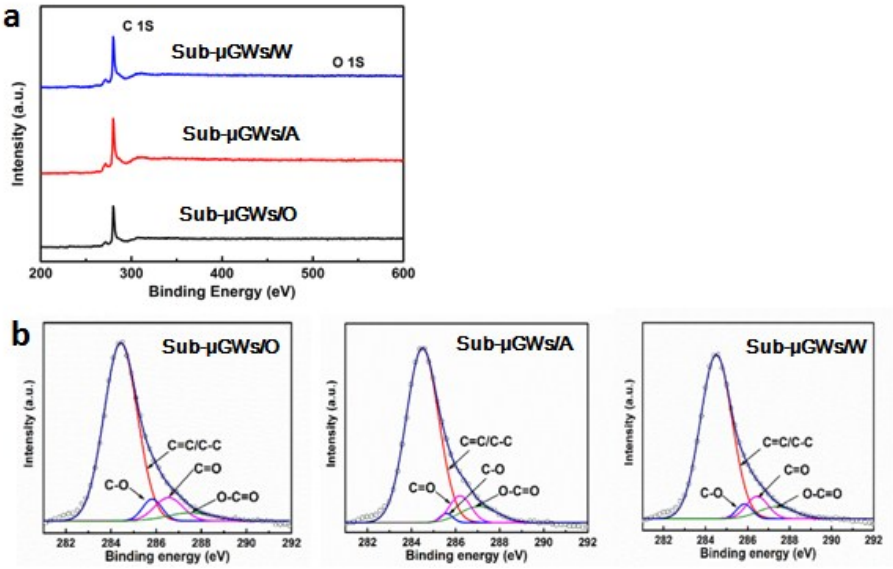

Fig. S7 (a) XPS survey spectra and (b) curve fit of C 1s spectra of Sub-μGWs.

The C 1s XPS spectrum was decomposed with a Gaussian fit, and five fractions were obtained, *i.e.*, the sp^2 and sp^3 hybridized carbon (C=C/C−C) at ~284.5 eV, the hydroxyl carbon (C−OH) at ~286.6 eV, the carbonyl carbon (C=O) at ~288 eV, and the carboxylate carbon (O=C−O) at ~289.9 eV, respectively. **Table S2** lists the fractions of C atoms in C=C/C−C, C−OH, C=O, and O=C−O, for Sub-μGWs/O, Sub-μGWs/A and Sub-μGWs/W samples.

Table S2. Fractions of C atoms in C=C/C−C, C−O, C=O, and O=C−O.

Samples	Items	C=C/C−C	C-O	C=O	O=C-O
Sub-μGWs/O	Binding Energy	284.5eV	285.6eV	286.2eV	287.1eV
	Fraction	81.28%	1.70%	8.35%	8.67%
Sub-μGWs/A	Binding Energy	248.4eV	285.8eV	286.5eV	287.5eV
	Fraction	80.29%	5.73%	8.90%	5.08%
Sub-μGWs/W	Binding Energy	284.5eV	285.8eV	286.5eV	287.3eV
	Fraction	81.86%	3.60%	7.70%	6.84%

S9. CV curve of Sub-µGWs/A electrode.

Fig. S8 a shows the CV curve of the Sub-µGWs/A electrode. The volumetric specific capacitance was calculated as 2.16 F/cm^3. Galvanostatic charge-discharge curves (current density of 10 A/g) of Sub-µGWs/A are presented in Fig. S8b

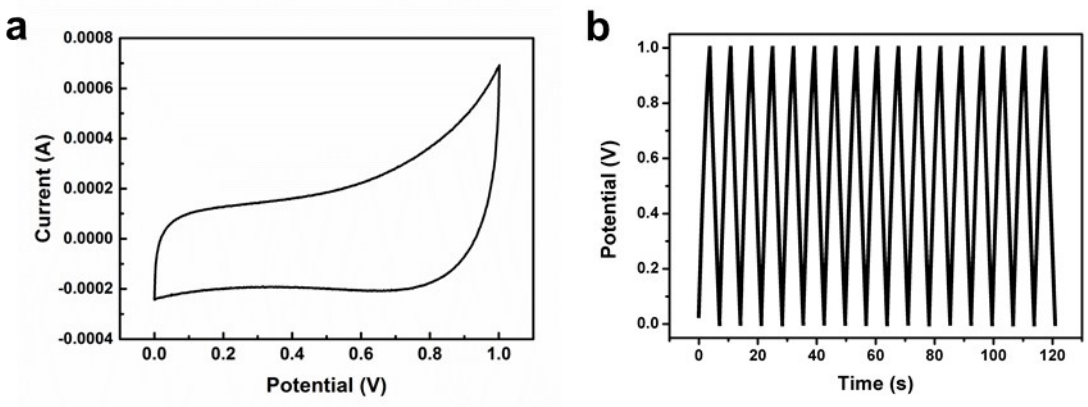

Fig. S8 (a) CV curve and (b) galvanostatic charge-discharge curves of Sub-µGWs/A electrode.

The galvanostatic charge-discharge curves in Fig. S8(b) show stable and highly-reproducible behavior which suggests that the chosen voltage window is suitable.

S10. Supercapacitors with different frequency responses.

Table S3. Supercapacitors with different frequency responses.

Active materials	Frequency for -45° phase angle	Ref.
Carbon nanoparticles/MnO_2 nanorods	2 Hz	SR6
Carbon nanotubes	~6 Hz	SR7
Vertically-oriented graphenes	41 Hz	SR8
Sub-μGWs/O	50 Hz	This work
Sub-μGWs/A	316 Hz	This work
Graphene oxide	~470 Hz	SR9
Hydrogen-treated carbon nanotubes	~500 Hz	SR10
Carbon black	641 Hz	SR11
Sub-μGWs/W	1258 Hz	This work
Vertically-oriented graphenes	15000 Hz	SR12

S11. Supporting references.

SR1. D. K. Owens and R. Wendt, *Journal of applied polymer science*, 1969, **13**, 1741-1747.

SR2. F. M. Fowkes, *The Journal of Physical Chemistry*, 1963, **67**, 2538-2541.

SR3. D. Khang, S. Y. Kim, P. Liu-Snyder, G. T. R. Palmore, S. M. Durbin and T. J. Webster, *Biomaterials*, 2007, **28**, 4756-4768.

SR4. A. Yarin, *Annu. Rev. Fluid Mech.*, 2006, **38**, 159-192.

SR5. T. Mao, D. Kuhn and H. Tran, *AIChE Journal*, 1997, **43**, 2169-2179.

SR6. L. Yuan, X.-H. Lu, X. Xiao, T. Zhai, J. Dai, F. Zhang, B. Hu, X. Wang, L. Gong, J. Chen, C. Hu, Y. Tong, J. Zhou and Z. L. Wang, *Acs Nano*, 2012, **6**, 656-661.

SR7. C. Du and N. Pan, *Nanotechnology*, 2006, **17**, 5314-5318.

SR 8. Z. Bo, Z. Wen, H. Kim, G. Lu, K. Yu and J. Chen, *Carbon*, 2012, **50**, 4379-4387.

SR 9. S. H. Aboutalebi, A. T. Chidembo, M. Salari, K. Konstantinov, D. Wexler, H. K. Liu and S. X. Dou, *Energy & Environmental Science*, 2011, **4**, 1855-1865.

SR 10. C. Du and N. Pan, *Journal of Power Sources*, 2006, **160**, 1487-1494.

SR 11. P. Kossyrev, *Journal of Power Sources*, 2012, **201**, 347-352.

SR 12. J. R. Miller, *Electrical Insulation Magazine, IEEE*, 2010, **26**, 40-47.